Improved Learning-Based approach for Atmospheric Compensation of VNIR-SWIR hyperspectral data

Nicola Acito, Member IEEE

***Abstract*— In this work, the Learning-Based approach to Atmospheric Compensation (LBAC) of hyperspectral data proposed in [19] is extended. LBAC makes use of machine learning methods to directly estimate the spectral reflectance from the at-sensor radiance accounting for the variability induced by one or more unknown atmospheric parameters and by-passing their estimation. LBAC training is obtained by exploiting a spectral reflectance library and accounting for the effects of both the atmosphere and the noise. However, depending on the spectral library adopted, some specific spectra may be reconstructed with lower accuracy. To overcome this drawback, two solutions are proposed referring to two application scenarios. The former deals with small and rare anomalous pixels with unknown reflectance and could be of interest in many applications such as man-made targets detection. It leverages the strengths of LBAC and those of the Empirical Line Method. The second scenario refers to the case of materials with a-priori known spectral reflectance and is defined for applications such as mining exploration and contaminant detection. It directly acts on the training phase of LBAC by introducing the spectra of interest in the generation of the training set.**

An extensive analysis is carried out on simulated data to test the effectiveness of the proposed solutions, to discuss their strengths and weakness, and to compare them with a classical physics-based approach. Results on a real hyperspectral image acquired by an airborne sensor provide a demonstration of the effectiveness of the proposed strategies in a real application environment.

***Index Terms*— Atmospheric compensation, Hyperspectral Imagery, Machine learning, Learning-based approach**

I. Introduction

Atmospheric compensation (AC) is one of the main issues to be addressed in hyperspectral remote sensing data exploitation. Data acquired by hyperspectral sensors refer to the spectral radiance of the observed objects/materials that must be transformed in the spectral reflectance domain in order to explore the physical and chemical composition of the observed surfaces. Such a transformation, called AC, aims at compensating the effects of the solar illumination and the distortion introduced by the atmospheric components in the path followed by the radiation ([1]-[7]). In general, AC is a very challenging task because the effects of solar illumination and atmosphere depend on several factors not directly measurable at the acquisition time.

In the VNIR (Visible and Near InfraRed)-SWIR (Short Wave InfraRed) spectral range, atmospheric effects mostly depend on a) the aerosol extinction, b) the absorption of uniformly mixed gases such as carbon dioxide (CO2), methane (CH4), oxygen (O2), and ozone (O3), c) the absorption of the water vapor ([7]). Aerosol extinction has a smooth spectral behavior and mainly depends on the particle size and distribution and on the visibility V (or equivalently on the Aerosol Optical Depth - AOD). It varies slowly in the spatial dimension and can be considered constant in relatively small scenes such as those acquired by aerial sensors.

CO2 and CH4 absorb radiation in the SWIR spectral range while O2 and O3 mainly influence the absorption in the VNIR spectral bands. These gases are relatively stable in concentration in both space and time and their absorption effects can be generally characterized by resorting to ancillary data.

Water absorption is due to the column water vapor concentration (CWV) in the downward and upward path and can be considered as the most significant distortion effect introduced by the atmosphere on the radiance measured by the sensor when the VNIR-SWIR spectral range is considered. Water vapor absorption is strong in specific spectral windows located in both the VNIR (around 720nm, 820 nm, 940 nm) and the SWIR (1130 nm, 1350 nm, 1850 nm, 2500 nm) spectral ranges. Its compensation is complicated by the high variability of CWV in both time and space domains also in small monitored areas ([6], [7], [8]).

Two general classes of AC methods are traditionally considered [9]: scene-based (SB) ([10], [11], [12]) and physics-based (PB) methods ([7], [13], [14], [15], [16], [17]). SB methods rely on empirical approaches and do not refer to the physics of radiation propagation through the atmosphere. Conversely, PB methods account for the physics of the radiative transfer in the atmosphere through a Radiative Transfer Model (RTM).

One of the most popular SB approaches is the Empirical Line Method (ELM - [11], [12]) which provides a prompt response to the AC problem by exploiting reference targets with known spectral reflectance deployed in the scene. Its use is limited by the need of such reference targets (not always available) and by its inability to address spatial nonstationary atmospheric

Manuscript submitted on May 21, 2021.

Nicola Acito is with Dipartimento di Ingegneria dell'Informazione, Università di Pisa, 56122 Pisa, Italy and also with Consorzio Nazionale Interuniversitario per le Telecomunicazioni (CNIT), 43124 Parma, Italy (e-mail: nicola.acito@unipi.it)

conditions (e.g. the variable CWV content of the atmosphere) and more complicated physical phenomena such as those due to adjacency effects.

In general, PB methods are more accurate and reliable of SB approaches. They perform AC without any *a priori* knowledge of the materials in the monitored scene and address the spatial variability of CWV by using estimation algorithms that work on a per-pixel basis. PB methods such as the Fast Line-of-Sight Atmospheric Analysis of Spectral Hypercubes (FLAASH, [15]) and the Airborne Atmospheric and Topographic Correction (ATCOR, [5]), have a two steps processing chain. First, RTM model parameters (mainly V and CWV) are estimated from the analyzed image. Then, those estimates are used to obtain the spectral radiometric quantities for RTM inversion and reflectance retrieval. Both steps exploit a specific Radiative Transfer Code (e.g. Modtran [18]) that relates the atmospheric model parameters to the spectral radiometric quantities.

In a recently published work ([19]), we introduced an approach alternative to SB and PB. It performs AC by using machine learning methods and directly estimate the spectral reflectance from the at-sensor radiance accounting for the variability induced by one or more unknown parameters of the RTM and by-passing the estimation step of the unknown atmospheric parameters. The approach is called Learning-Based Atmospheric Compensation (LBAC) because it uses a parametric regression function whose parameters are determined through a specific learning strategy. The latter exploits simulated data that account for the variability of both the atmosphere and the surface spectral reflectance. Furthermore, the learning method is specifically designed to take noise into account in order to make the regression function robust to its effects. LBAC is quite general and different forms of parametric regression functions can be adopted and learned to accomplish the AC task, including those characterized by complex architectures such as deep neural networks. In [19], a first function based on multilinear regression was proposed and tested over real airborne hyperspectral. Results showed the effectiveness of the method and encouraged further analysis and developments within the framework of the Learning Based approach.

The learning-based approach exploits the spectra contained in a library for two different purposes: a) subspace coding of the spectral reflectances and b) construction of the training set. In [19] an extensive spectral library containing more than a thousand spectra from different natural (vegetation, soils, water and minerals) and man-made materials was adopted. The spectral library was obtained merging three different publicly available spectral databases: ASTER ([20]), USGS (version released in 2007, [21]) and Lopex and Angers ([22]). All the signatures in the considered library have a slower rate of change in the spectral domain than that typically exhibited by the radiance data which is mainly due to atmospheric effects and noise. This characteristic of the reflectance spectra included in the adopted library is shared by many natural surfaces and man-made materials, as evidenced by several authors ([23], [24]) and experimental measures ([25]). The "regular" behavior of the spectra in the library, together with the specific learning strategy adopted by LBAC, makes the approach quite effective in many application fields such as land use/land cover, water quality, basic mineralogical analyses and some terrestrial and aquatic ecosystem investigations. In addition, they provide LBAC with an intrinsic polishing capability that guarantees a certain degree of robustness to mis-calibration errors and noise. This polishing effect may be less effective when one is interested in materials whose spectrum cannot be represented as a linear combination of the spectra in the adopted library. In fact, in this case, one risks losing the features that allow discrimination of that material. Despite the library is highly populated and the learning strategy designed to properly account for all the library items, it may happen that some spectra encountered in the analyzed image are reconstructed with lower accuracy. We will denote these spectra as *anomalous*, hereinafter. For example, anomalous spectra can be associated to the presence of specific narrowband spectral features. In general, anomalous spectra represent a very small fraction of the pixels of the image and the reflectance retrieved by LBAC can be effectively used for classification and recognition tasks.

In specific applications one may be interested in detecting, recognizing or, in general analyzing, *anomalous* materials. For example, this might be the case of the detection/analysis of specific environmental contaminants and canopy chemistry, which may exhibit narrowband spectral features, but also it might be the case of man-made target detection applications, where the spectral signature of the target of interest may be not properly described by the learning procedure.

However, LBAC is a quite general approach, and most of the limitations related mainly to the library adopted for subspace coding and training, in specific application scenarios, can be overcome by *ad-hoc* changes or additions to the procedure.

In this work we present two different strategies to make LBAC suitable for those applications interested in anomalous spectral features. Specifically, we consider two operational scenarios.

The first concerns objects/materials having anomalous spectral features and a small spatial extent. A typical example of application included in this scenario is the detection and recognition of man-made targets (vehicles, specific paints, concealing materials, etc.). The exact meaning of the term "small" will be clarified in the next sections. The second proposed strategy focuses on applications where the material of interest has known anomalous reflectance and does not necessarily have a small extent in the spatial dimension. It could be the cases of mineralogical applications and specific contaminants analysis.

This paper is organized as follows. In Section II, we recall the basics of the LBAC approach. In Section III, we detail the two strategies for improving LBAC performance with reference to the operational scenarios previously introduced. Then in Section IV, we demonstrate the effectiveness of the proposed improvements and we discuss their strengths and weaknesses on simulated images. Finally, we present and discuss results on a real hyperspectral image (Section V). Concluding remarks are reported in Section VI.

II. LBAC ALGORITHM

To summarize the learning-based approach we start by introducing the RTM we refer to.

Assuming the observed surface as Lambertian, the at-sensor radiance vector $\mathbf{L}\epsilon R^{N_B}$ on the N_B hyperspectral sensor channels, is expressed as ([7]):

$$\begin{aligned}\mathbf{L}(\boldsymbol{\rho},\boldsymbol{\rho_a},\boldsymbol{\Gamma}) &= \mathbf{L}_{GND}(\boldsymbol{\rho},\boldsymbol{\rho_a},\boldsymbol{\Gamma}) + \mathbf{L}_p(\boldsymbol{\Gamma}) \\ \mathbf{L}_{GND}(\boldsymbol{\rho},\boldsymbol{\rho_a},\boldsymbol{\Gamma}) &= \frac{\mathbf{E}cos(\vartheta_s)}{\pi}[\boldsymbol{\tau}_1(\boldsymbol{\Gamma})\frac{\boldsymbol{\rho}}{1-\mathbf{S}(\boldsymbol{\Gamma})\boldsymbol{\rho_a}} \\ &\quad + \boldsymbol{\tau}_2(\boldsymbol{\Gamma})\frac{\boldsymbol{\rho_a}}{1-\mathbf{S}(\boldsymbol{\Gamma})\boldsymbol{\rho_a}}]\end{aligned} \quad (1)$$

where $\mathbf{L}_{GND}$ denotes the ground reflected radiance, i.e.: the contribution of the solar radiation that after the interaction with the surface is captured by the sensor. For the sake of conciseness, the description of the radiometric quantities in eq. (1) is summarized in Table 1, the meaning of the rest of the symbols in eq. (1) is briefly explained below:

- the symbol ϑ_s denotes the sun zenith angle;
- the vector $\boldsymbol{\Gamma}$ groups all the parameters that specify the acquisition conditions (acquisition geometry and atmosphere). Many of them, are generally known when AC task is performed. Specifically, we refer to all the parameters related to the acquisition geometry and to the concentration of gases that are relatively stable in the spatial and time domains. As specified in Section I, the most significant unknown atmospheric parameters that, strictly depend on the specific monitored scene and need to be properly accounted for in performing the AC task, are V and CWV.
- $\mathbf{L_a}$ is the spectral radiance from adjacent regions. It is assumed known and modelled as $\mathbf{L}_{\boldsymbol{a}}(\boldsymbol{\rho_a},\boldsymbol{\Gamma}) = \mathbf{L}(\boldsymbol{\rho_a},\boldsymbol{\rho_a},\boldsymbol{\Gamma})$, i.e. by applying eq. (1) to the case of $\boldsymbol{\rho} = \boldsymbol{\rho_a}$ ([7]). It is, generally, obtained from the analyzed data ([6], [5]) by applying a linear and space invariant filter whose impulse response approximates the atmospheric Point Spread Function (PSF).

In real applications, the observed at-sensor radiance vector is corrupted by noise that can be modelled as an additive term $\mathbf{N}\epsilon R^{N_B}$. It includes, spectral and radiometric miscalibration errors and both the thermal and the photon random noises.

LBAC estimates $\boldsymbol{\rho}$ directly from the at-sensor (noisy) radiance $\mathbf{L}$ of the observed pixel and that from adjacent regions $\mathbf{L_a}$ regardless of the spatially varying values of CWV, and without the calculation of the radiometric quantities. It assumes the knowledge of V that is obtained through a procedure based on dark pixels ([19]) which can be applied globally or locally depending on the spatial extension of the monitored scene.

The general formulation of the learning-based approach is summarized in the block diagrams of Figure 1 (a) and (b). The procedure considers the use of a compact representation for the spectral reflectance domain. It aims to limit overfitting, reduce the computational load and filter out unwanted effects (e.g. noise). Thus, the spectral reflectance vector $\boldsymbol{\rho}$ is represented by means of a code $\mathbf{c}$. In the block diagrams of Figure 1 (a) and (b) the blocks called "encoder" and "decoder" perform the transformation of the reflectance in the compact domain and its inverse, respectively.

Table 1. Description of the radiometric quantities in eq. (1).

$\mathbf{L}_{GND}(\boldsymbol{\rho},\boldsymbol{\rho_a},\boldsymbol{\Gamma})$	GrouND reflected radiance: spectral radiance reaching the sensor after the interaction with the surface.
$\mathbf{L}_p(\boldsymbol{\Gamma})$	Intrinsic upwelling atmospheric spectral radiance
$\boldsymbol{\rho}$	Surface spectral reflectance
$\boldsymbol{\rho}_a$	Spectral reflectance from background (adjacent surfaces)
$\mathbf{E}$	Solar spectral irradiance at the top of the atmosphere
$\boldsymbol{\tau}_1(\boldsymbol{\Gamma})$	Spectral transmittance: radiometric quantity accounting for the interaction of the surface material with the direct and diffuse solar radiation
$\boldsymbol{\tau}_2(\boldsymbol{\Gamma})$	Spectral transmittance from adjacent pixels: radiometric quantity accounting for the part of the solar radiation that, after the interaction with the materials in a neighborhood of the surface of interest, is scattered by the atmosphere in the sensor Instantaneous Field Of View
$\mathbf{S}(\boldsymbol{\Gamma})$	Spectral spherical albedo of the atmosphere

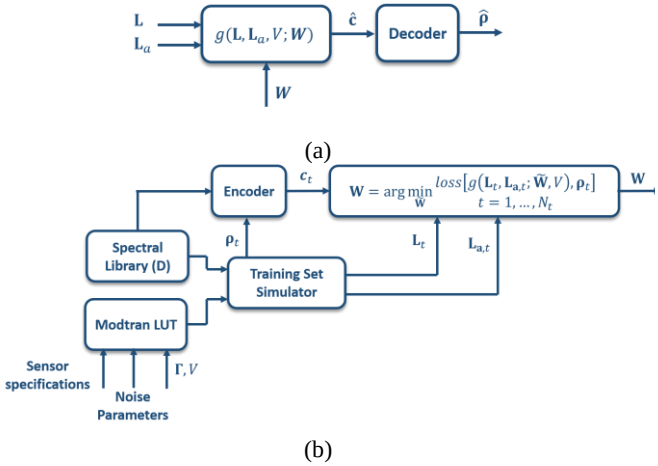

Figure 1. Block diagrams of the learning based approach to AC: (a) application of the method to the image pixels; (b) learning mechanism.

Figure 1 (a) refers to the regression system that is based on the model $g(.;\boldsymbol{W})$ (the parametric regression function). It applies to the at sensor radiance vector $\mathbf{L}$ and the adjacent radiance vector $\mathbf{L}_a$ associated to each image pixel, and provides as output the code $\hat{\boldsymbol{c}}$ that, then, is transformed (decoded) in the estimate of the spectral reflectance $\hat{\boldsymbol{\rho}}$.

The regression model $g(.;\boldsymbol{W})$ depends on the set of parameters $\boldsymbol{W}$ that is "learned" by the training mechanism depicted in Figure 1 (b). Specifically, $\boldsymbol{W}$ is the result of the minimization of a given loss function over the training set triplets $\{\boldsymbol{c_t}, \mathbf{L_t}, \mathbf{L_{a,t}}\}$ with $t = 1, \ldots, N_T$, which are generated through simulation. Here N_T is the total number of training triplets.

Each triplet is obtained starting from a couple of vectors $\boldsymbol{\rho_t}$ and $\boldsymbol{\rho_{a,t}}$ generated by applying the Linear Mixture Model (LMM) to randomly selected elements of a spectral library $\mathbf{D}$. The number of endmembers and the mixture coefficients are also randomly generated. The first element of each triplet is the code $\boldsymbol{c_t}$ of $\boldsymbol{\rho_t}$. From, $\boldsymbol{\rho_t}$ and $\boldsymbol{\rho_{a,t}}$ several pairs of radiance and adjacent radiance

vectors are generated. Each pair $\{\mathbf{L}_t, \mathbf{L}_{a,t}\}$ completes a training triplet including $\boldsymbol{c_t}$. The spectral radiance vectors are obtained by combining $\boldsymbol{\rho_t}$ and $\boldsymbol{\rho_{a,t}}$ according to the adopted RTM (eq. (1)), with the radiometric quantities generated by Modtran ([18]) varying CWV as a uniformly distributed random variables in the range $[0.5, 5]\ g \cdot cm^{-2}$. The rest of the atmospheric and geometric parameters are kept constant. The generated radiances are mapped in the sensor spectral domain by accounting for the specific Spectral Response Function of the sensor channels. Furthermore, mis-calibration errors and random noise (with different values of the Signal to Noise Ratio) are added to the radiance vectors. This aims to account for those sources of disturbance in the learning mechanism so as to provide the AC algorithm with a certain degree of robustness with respect to them.

The schemes in Figure 1 (a)-(b) define the general class of LBAC algorithms, each of one is fully specified by the encoding/decoding strategy, the regression model, and the adopted spectral library **D**.

In the specific case of the LBAC algorithm analyzed and tested in [19], reflectance encoding is performed through subspace projection using a basis matrix **U** derived from **D** by a procedure based on the Singular Value Decomposition (SVD). The regression model, has the form of a multilinear regression:

$$\begin{gathered}\hat{\mathbf{c}} = \mathrm{g}(\mathbf{L}, \mathbf{L}_a, V, \mathbf{W}) = \mathbf{W}(V)^T \cdot \mathbf{x} \\ \mathbf{x} = [\mathbf{L}^T, \mathbf{L}_a^T, 1]^T\end{gathered} \tag{2}$$

Of course, the reflectance estimate is obtained by inverting (decoding) the subspace coding, i.e. $\hat{\boldsymbol{\rho}} = \mathbf{U} \cdot \hat{\mathbf{c}}$.

The loss function (eq. (3)) adopted in the training mechanism, is the squared relative error averaged over the entire training set. An additive $L2$ regularization term is introduced to limit overfitting and avoid ill-conditioning.

$$\begin{gathered}loss\left[\widetilde{\mathbf{W}}; \mathbf{x_t}, \mathbf{c}_t, V\right] = \\ t = 1, \ldots, N_T \\ = \sum_{t=1}^{N_t} \frac{\left\|\mathbf{c}_t - \widetilde{\mathbf{W}}(V)^T \cdot \mathbf{x_t}(V, CWV)\right\|^2}{\|\mathbf{c}_t\|^2} + \beta \left\|\widetilde{\mathbf{W}}(V)\right\|_F^2\end{gathered} \tag{3}$$

In eq. (3) $\|\ \|$ and $\|\ \|_{\mathrm{F}}$ denote the $L2$-norm and the Frobenius norm, respectively. The weight β of the regularization term is learned from training data by K-fold cross-validation.

As a general comment about the learning-based approach, we can state that spectral features that are not correctly encoded by the adopted encoding strategy and/or not sufficiently represented in the reflectance spectra adopted in the training set, are ignored by the LBAC algorithm. Those spectral features will be referred to as "anomalous", hereinafter.

In the specific case of the LBAC algorithm detailed in [19], the use of subspace projection as a coding strategy and the LMM to construct the reflectance spectra in the training set, leads to the conclusion that the algorithm fails in estimating spectral features that cannot be obtained as a linear combination of the spectra included in the adopted library. The library adopted in [19] is that introduced in Section I which contains many natural and man-made materials characterized by a "smooth" behavior. As stated in Section I, here the term smooth refers to the fact that the reflectance spectra have a change rate lower than that characterizing the corresponding radiance and basically due to atmospheric effects and noise. As a consequence, the algorithm is expected to provide poor performance for the spectra that have rapid changes in the spectral domain. For example, are anomalous those materials or surfaces characterized by narrow band spectral features. In some applications, this is a limitation of LBAC algorithm, because the features not represented are the most significant for the problem being addressed.

III. LBAC IMPROVEMENTS

In this section, we propose two possible solutions for the above introduced problem, in the case of LBAC algorithm proposed in [19] and concerning two distinct operational scenarios. The two scenarios will be referred to as "small and rare anomalies" and "anomalies with known spectral reflectance" in the rest of the paper.

A. Small and rare anomalies scenario.

The first scenario refers to the case of anomalous materials/surfaces that are small in spatial extent and scarcely present (rare) in the scene. This scenario is typical for target detection applications, where one is interested to detect civilian or military vehicles and/or specific paints or minerals, which are deployed in small portions of the scene. Of course, it applies to those cases in which *a-priori* information is available on the spatial extent (relative to the GSD) of the targets of interest. Spectral target information is not necessary.

Starting from the consideration that LBAC provides a good approximation for the reflectance of most of the image pixels, we propose a strategy that combines LBAC with the ELM and leverages the strengths of the two approaches.

ELM assumes a simple linear relationship between the radiance and the reflectance in each sensor channel, that can be viewed as the simplified version of the RTM in eq. (1) where the adjacency effects are neglected (or considered constant all over the image). The linear coefficients for each sensor channel, are estimated by exploiting at least two reference targets deployed in the scene with known and different spectral reflectances. The use of more reference targets in conjunction with Ordinary Least Square (OLS) improves the robustness of the algorithm to random noise in estimating the linear model coefficients. Of course, the inversion of the linear model for reflectance derivation, carries with it the random noise instance presents in the measured radiance. ELM is inherently robust to systematic errors in the image such as those due to imperfect radiometric and/or spectral calibration.

It is worth noting that, ELM does not account for the spatial variability of CWV because it accounts for the CWV effects only in the region of the scene where the reference targets are deployed. In addition to the limitations related to its inability in addressing spatially variant atmospheric effects, the use of ELM is strongly limited by the need of the reference targets. In many satellite and airborne applications, the assumption of the availability of reference targets is unlikely to be satisfied.

However, the strengths of ELM can be exploited in the

considered scenario as a post-processing of the results provided by LBAC algorithm. Let us focus on the pixel in the position (i,j) of the image and denote as $\Omega_{i,j}$ the neighborhood centered in (i,j). Assume that $\Omega_{i,j}$ is small enough to consider both the adjacency effects and CWV constant inside. For $\forall\ (k,n) \in \Omega_{i,j}$, in the b-th sensor channel the RTM in eq. (1) can be rewritten as:

$$\begin{aligned} L_b(k,n) &= A_{i,j,b} \cdot \rho_b(k,n) + C_{i,j,b} + N(k,n) \\ A_{i,j,b} &= \frac{\mathrm{E}_b cos(\vartheta_s)}{\pi} \frac{\tau_{1,b}(\bar{\mathbf{\Gamma}})}{1 - \mathrm{S}_b(\bar{\mathbf{\Gamma}})\bar{\rho}_{a,b}} \\ C_{i,j,b} &= \frac{\mathrm{E}_b cos(\vartheta_s)}{\pi} \frac{\tau_{1,b}(\bar{\mathbf{\Gamma}}) \cdot \bar{\rho}_{a,b}}{1 - \mathrm{S}_b(\bar{\mathbf{\Gamma}})\bar{\rho}_{a,b}} + \mathrm{L}_{p,b}(\bar{\mathbf{\Gamma}}) \end{aligned} \quad (4)$$

where $\bar{\mathbf{\Gamma}}$ is the vectors of constant atmospheric parameters (CWV is constant in $\Omega_{i,j}$) and $\bar{\rho}_{a,b}$ is the b-th element of the adjacent reflectance vector assumed as constant in $\Omega_{i,j}$. The terms $N(k,n)$ accounts for the noise.

Eq. (4), shows that for all the pixels in $\Omega_{i,j}$, and in each sensor channel, the RTM in eq. (1) coincides with the linear model assumed by ELM. Thus, in that neighborhood, ELM can be applied to derive $A_{i,j,b}$ and $C_{i,j,b}$ with the reflectance estimates obtained by LBAC acting as known references. Of course, the values of the reflectance in (i,j) is obtained by inverting the model. $A_{i,j,b}$ and $C_{i,j,b}$ are derived by OLS with an additive regularization term. In formulas, $A_{i,j,b}$ and $C_{i,j,b}$ minimize:

$$\sum_{(k,n)\in\Omega_{i,j}} \left[L_b(k,n) - A_{i,j,b} \cdot \rho_b(k,n) - C_{i,j,b}\right]^2 + \mu \cdot \left(\bar{L}_{p,b} - C_{i,j,b}\right)^2 \quad (5)$$

where $\bar{L}_{p,b}$ is the intrinsic upwelling atmospheric spectral radiance averaged with respect to CWV and it is obtained by the Look Up Table (LUT) derived by Modtran and adopted in the training of the LBAC algorithm. The regularization terms based on $\bar{L}_{p,b}$ is introduced to avoid ill-conditioning in the case of fully homogeneous neighborhood, i.e.: all the reflectances in $\Omega_{i,j}$ have the same value[1]. In the implementation of the method tested in the next Sections, we set $\mu = 1$ that gives to the regularization factor the same weight as all the samples in $\Omega_{i,j}$. Alternative choices could be considered that take into account, for instance, the variability of the reflectances with respect to the noise variance.

Notice that, with a sufficiently large neighborhood, the reflectance of the material in the pixel (i,j) does not influence the estimates $A_{i,j,b}$ and $C_{i,j,b}$. Thus, if that spectrum is anomalous, it is correctly reconstructed by inverting the model.

Of course, the previously described operations are applied to all the sensor channels and all the image pixels by using a classic moving window scheme. In some applications, post-processing can be applied to few pixels, i.e. those detected by an anomaly detection algorithm carried out on the radiance image.

Now, we can specify what we mean by small anomalies in the definition of this scenario. Small anomalies are those that do not introduce bias in the estimation of the linear model coefficients $A_{i,j,b}$ and $C_{i,j.b}$. So, they have a spatial extension much lower than that of $\Omega_{i,j}$. The size of $\Omega_{i,j}$ should be as high as possible, not only to limit the aforementioned bias, but also to limit the effects of random noise on the estimates of the linear coefficients, and to avoid ill-conditioning due to the low variability of the enclosed reflectance spectra. On the other hand, the size of $\Omega_{i,j}$ has an upper bound related to the need of satisfying the assumption of constant values for CWV and the adjacent reflectance. In general, this assumption is satisfied in regions of the scene of several meters. Accordingly, the feasibility of the proposed method is related to the sensor spatial resolution.

LBAC with ELM based post-processing, as in the case of original ELM, provides reflectance estimates that include the random noise instance for each image pixel. However, it still retains robustness to systematic errors due to incorrect radiometric and spectral calibration. We will give evidence of the previous assertion in Section IV.

The strategy described in this sub-Section will be referred to as LBAC with ELM (LBAC-ELM, for short) in the rest of the paper.

B. Anomalies with known spectral reflectance scenario.

This scenario refers to the materials/surfaces whose anomalous spectral reflectance is *a priori* known. In this case, the targets of interest do not have to be small and rare as in the previous scenario. It applies to some practical problems such as those related to the detection of contaminants and minerals characterized by specific absorption features and present in relatively large regions of the scene. It is worth noting that, one of the applications enabled by the availability of the spectral reflectance data is the recognition/identification of specific materials. The recognition/identification task is performed by comparing the image data (reflectance) with the spectral reflectance of the material of interest that, obviously, must be known. It is generally obtained from laboratory or in situ measurements.

The solution proposed for this scenario acts directly on a) the coding strategy and b) the learning strategy of the LBAC algorithm presented in [19].

Let us start by considering the case of a single anomalous target with (known) spectral reflectance $\boldsymbol{\rho}^*$. The first modification is made on the basis matrix $\mathbf{U}$. It consists in using $\boldsymbol{\rho}^*$ as an additional basis vector thus obtaining the new basis matrix $\mathbf{U}^* = [\mathbf{U}, \boldsymbol{\rho}^*]$. This change allows for coding of the anomalous spectrum. Then, the training set is modified in order to allow the learning of the new codes derived by the modification of the basis matrix. Specifically, it is changed with the dual purpose of 1) preserving the ability of the system to represent typical man-made and natural materials (those obtained by the original library) and 2) giving it the ability to deal with the new anomalous feature. To this end, two classes of spectral reflectances are generated for the construction of the training set: one representative of the data in the library (background class) and the other including the anomalous spectral feature (anomaly class). Both are generated according to the LMM by

[1] Notice that, regularization term is a condition less strong than $\bar{L}_{p,b} = C_{i,j}$ which would not satisfy the model in eq. (4).

the procedure recalled in Section II.

$$\boldsymbol{\rho}_t^{BKG} = \sum_{i=1}^{N} a_i \mathbf{d}_i$$
$$\boldsymbol{\rho}_t^{AN} = \sum_{i=1}^{N-1} a_i \mathbf{d}_i + a^* \boldsymbol{\rho}^* \quad (6)$$

According to eq. (6), the spectra of the background class and those of the anomaly class are generated as a linear combination of a given set of spectral reflectances (called endmembers) taken from the library **D**.

Specifically, for the generic reflectance of the background class $\boldsymbol{\rho}_t^{BKG}$, the generation is the same as that used in the original version of LBAC. The endmembers $\mathbf{d}_i$ are randomly selected from the library **D** and the mixture coefficients a_i are drawn according to the Dirichlet distribution so as to meet the sum-to-one and the non-negative constraints. For the reflectance of the anomaly class $\boldsymbol{\rho}_t^{AN}$, one of the endmembers is constrained to be $\boldsymbol{\rho}^*$ and the remaining $N-1$ are selected randomly from **D**. Furthermore, the coefficient a^* of $\boldsymbol{\rho}^*$ is generated as uniformly distributed in $[0.5,1]$ and the rest according to the sum-to-one and the non-negative constraints. The total number N_T of training triplets are generated so as to contain the same number of elements of the two classes.

The generalization of the procedure to N_A anomalous reflectances $\boldsymbol{\rho}_i^*$ $(i = 1, \dots, N_A)$ is obtained straightforwardly by iterating the steps previously describe.

The proposed strategy, thanks to both the coding and the learning mechanism, preserves the robustness of LBAC to systematic and random noise sources. However, this property weakens as the number N_A of the anomalous reflectances increases. Specifically, as the rank of the reflectance subspace increases due to the addition of N_A anomalous spectra, the number of random noise components included in that subspace also increases, reducing the system's ability to filter out the noise itself. In addition, the risk that the system considers spectral features of the radiance data due to atmospheric effects or various systematic errors, useful for estimating the spectral reflectance, also increases.

The strategy described in this sub-Section will be referred to as LBAC with Known spectral reflectance (LBAC-K for short) in the rest of the paper.

It is worth noting that, LBAC-K also applies to small and rare anomalies as long as their spectral reflectances are known

IV. Results on Simulated Data

In this Section the effectiveness of both LBAC-ELM and LBAC-K defined in Section III is demonstrated on data simulated according to the operational scenarios to which the two methods refer.

Simulated data are obtained by a strategy that includes three main steps. First, starting from a given reflectance image we inject specific anomalous targets into randomly selected positions. Then, according to the RTM in eq. (1), we simulate the radiance image by accounting for the atmospheric effects. Finally, random noise and spectral calibration errors are added to the radiance image. In the following, each step of the simulation strategy is described in depth.

The reflectance image adopted in our simulations is obtained by applying the LBAC algorithm in [19] to a publicly available hyperspectral image which is part of the SHARE 2012 data set from the Digital Imaging and Remote sensing Laboratory of the Rochester Institute of Technology ([26], [27]). Specifically, the image is one of those presented in [19] to show the results of LBAC on real data.

The image, whose Red Green Blue (RGB) representation is shown in *Figure 2* (a), was acquired on 20 September, 2012 at 15:46 (GMT), in a rural scene located in AVON, New York, just south of Rochester. It was collected by ProSpecTIR VS system, a hyperspectral airborne pushbroom spectrometer operating in the VNIR and SWIR (400-2400 nm) spectral ranges and having 360 spectral bands with spectral resolution of 5 nm. It was acquired with a spatial resolution lower than 1 m. The total number of pixels in the image is 340x450.

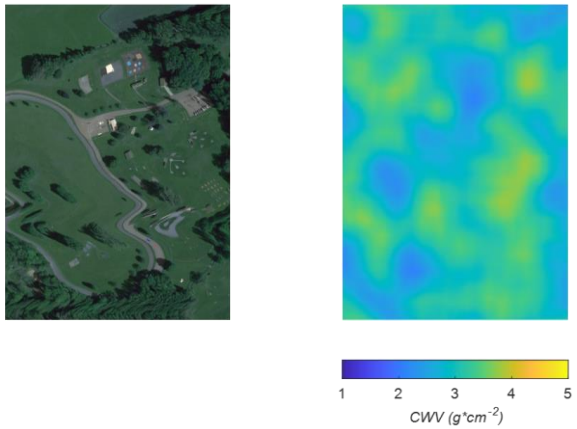

Figure 2. (a) RGB representation of the reflectance image adopted for simulating the data; (b) example of simulated CWV map.

Such a reflectance image represents the background of the simulated scene where, in each experiment, we inject specific anomalous targets. Each anomalous target is obtained simulating a narrow band spectral feature on the reflectance spectrum of a randomly selected pixel of the background. Specifically, denoted as $\boldsymbol{\rho}_{s,l}$ the reflectance of the pixel in the (randomly) selected image coordinates (s,l), the anomalous spectrum is obtained as:

$$\boldsymbol{\rho}_{s,l}^{AN} = (1 - \boldsymbol{\delta}) \cdot \boldsymbol{\rho}_{s,l}$$
$$\delta_b = A \cdot exp\left[-\frac{(\lambda_b - \bar{\lambda})^2}{2\bar{\sigma}^2}\right] \quad b = 1, \dots, N_B \quad (7)$$

where b denotes the sensor channel, δ_b is the value of $\boldsymbol{\delta}$ in the b-th sensor channel, λ_b is the central wavelength of the b-th sensor channel. Eq. (7) shows that, the vector $\boldsymbol{\delta}$ introduce a gaussian shaped distortion on $\boldsymbol{\rho}_{s,l}$, centered at the wavelength $\bar{\lambda}$, with depth A and whose width is determined by $\bar{\sigma}$. The three parameters of the gaussian distortion are randomly generated. $\bar{\lambda}$ is generated according to a uniform distribution in the spectral range covered by the sensor channels (400-2400 nm), the wavelengths falling in the strongest water absorption spectral

windows around 1400 nm and 1850 nm are discarded. $\bar{\sigma}$ is obtained as $\bar{\sigma} = K \cdot FWHM$, where $FWHM$ represents the average Full Width Half Maximum of the ProSpecTIR VS sensor and K is uniformly distributed in the range [1,5] in order to generate narrow spectral features in accordance with the sensor spectral resolution. The depth A is generated as a random variable uniformly distributed in the range $[0.5, 0.8]$. Examples of simulated anomalous spectra are shown in Figure 4 (b)-(c).

Of course, anomalous targets with different size (in pixels) can be generated depending on the operational scenario to be simulated.

The reflectance image (including anomalous targets) is transformed in the radiance domain by accounting for the atmosphere, the sensor specifications, the random noise and the systematic errors. The spectral reflectances accounting for the adjacency effects ($\boldsymbol{\rho_a}$) are obtained by linear filtering the reflectance image.

As to the atmospheric effects, the RTM in eq. (1) is considered and the radiometric quantities are generated by Modtran. The parameters that define the geometrical and atmospheric conditions are also randomly generated. In Table 2 we specify the range of variation for the simulation of some of the considered parameters. In all the experiments, without loss in generality, nadir viewing is assumed.

In order to account for different aerosol conditions, three standard Modtran aerosol models are considered in our simulations: urban, rural and navy maritime. They are randomly chosen in each simulated image.

In order to account for CWV spatial variability, we generate a CWV map having the same size of the original reflectance image. It is obtained starting from a white gaussian process with mean value μ_W drawn from a uniform distribution in the range [0.5,4.5] g/cm^2 and standard deviation $\sigma_W = 0.1\mu_W$. To simulate the spatial correlation, linear filtering is applied to the map. As an example, in *Figure 2* b) we show a CWV map obtained with $\mu_W = 3\ g/cm^2$.

Table 2. List of parameters for acquisition condition and their range of variation

Parameter	Range of values (lower bound, upper bound)
Sensor height	0.5, 3 km
Solar zenith angle	0, 40 deg
Visibility (V)	10, 90 km

Noise is then added to the radiance image to simulate both random noise and errors due to imperfect data calibration. Specifically, random noise is generated according to the model in [28] and [29]. It takes into account both the photon and the thermal noise components. The noise power is quantified and changed by means of the SNR parameter. As to SNR values, three cases are considered: a) $SNR = 30\ dB$, b) $SNR = 35\ dB$ and c) $SNR = 50\ dB$. In Figure 3, just to give an example, for a pixel taken from one of the roads in the image, we plot, in the three cases, the noisy Top Of the Atmosphere (TOA) reflectance, i.e. that obtained by dividing the at-sensor radiance by the solar spectral irradiance **E** (eq. (1)). The interested reader is referred to [19] for more details about the random noise simulation procedure.

As to the mis-calibration errors, in this work only those due to imperfect spectral calibration are considered. They are simulated by introducing a spectral shift proportional to the $FWHM$ in the central wavelength of all sensor channels. Details about the amount of the spectral shift will be provided in the discussion of the results.

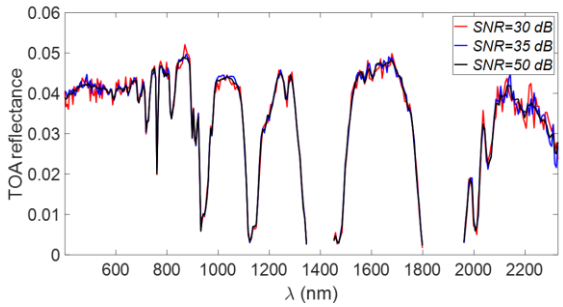

Figure 3. Noisy Top Of the Atmosphere (TOA) reflectance for a pixel taken on the road with three different values of SNR.

In all the experiments presented in this Section, the original version of LBAC algorithm makes use of a basis matrix (**U**) with rank 40 and is trained by $N_T = 10^5$ training triplets. Performance of the algorithms are evaluated in terms of root relative squared error. For the pixel with spatial coordinates (s, l) it is defined as:

$$\mathrm{E}_{s,l}^{ALG} = \frac{\left\|\boldsymbol{\rho}_{s,l} - \hat{\boldsymbol{\rho}}_{s,l}^{ALG}\right\|}{\left\|\boldsymbol{\rho}_{s,l}\right\|} \tag{8}$$

where the superscript ALG denotes the specific AC algorithm adopted, $\boldsymbol{\rho}_{s,l}$ is the true reflectance vector and $\hat{\boldsymbol{\rho}}_{s,l}^{ALG}$ is its estimate provided by the ALG algorithm.

A. LBAC-ELM performance analysis.

We start our discussion from the first scenario ("small and rare anomalies") that is obtained by simulating the radiance images according to the previously described procedure with reflectance images obtained by randomly injecting in the background, 50 anomalous spectra with size 3x3 pixels. These images are processed by LBAC and LBAC-ELM. The latter has a single parameter to be specified that is the size of the neighborhood. In all the experiments, according to a) the remarks at the end of Sub-Section III.A, b) the dimension of the simulated anomalies (3x3 pixels) and c) considering that the GSD of the simulated data is of about 1 m, we set the size of the neighborhood to 11x11 pixels. This corresponds to a region of the scene with spatial extent of 11 m x 11 m, where CWV values and adjacent effects can be reasonable considered constant.

In order to provide a more complete analysis and discussion we have also applied a PB algorithm, which uses the same visibility estimate adopted by the two LBAC versions and CWV

estimates provided by the well-known Atmospherically Pre-corrected Differential Absorption technique (APDA) proposed in [8]. APDA is applied to the water absorption spectral window around 940 nm. The PB algorithm will be referred to as PB-APDA, hereinafter.

As a first example, in Figure 4 (a)-(c) we show the results provided by the three algorithms on one background pixel from vegetation (Figure 4 (a)) and two anomalous pixels (Figure 4 (b)-(c)) in one of the simulated radiance images. In each figure we also plot the true spectrum. The figures were obtained with $SNR = 30\ dB$ and in the absence of spectral calibration errors (the spectral shift is 0). In addition to the reflectance spectra, the figures show the atmospheric absorption spectral windows due to water vapor (transparent blue patches), CO2 and CH4 and, for the anomalous pixels, the central wavelengths of the simulated narrow band spectral features (red dashed vertical line).

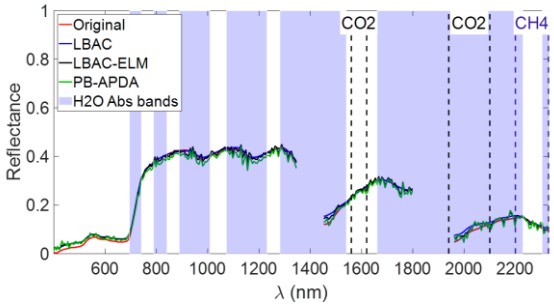

(a)

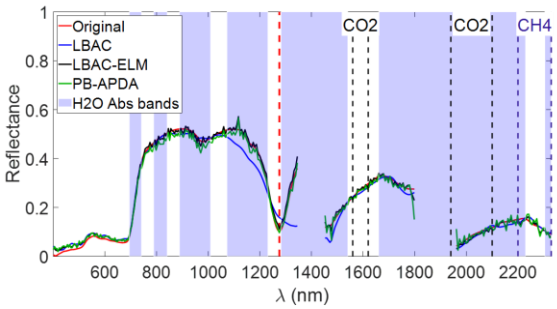

(b)

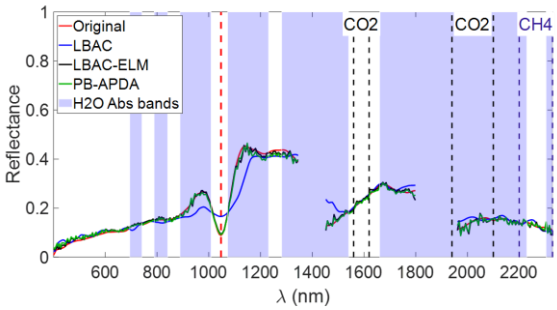

(b)

Figure 4. Examples of estimation provided by LBAC, LBAC-ELM and PB-APDA on three spectra: (a) background; (b) anomalous spectrum 1 and (c) anomalous spectrum 2. In this case SNR=30 dB and in the absence of a systematic spectral shift.

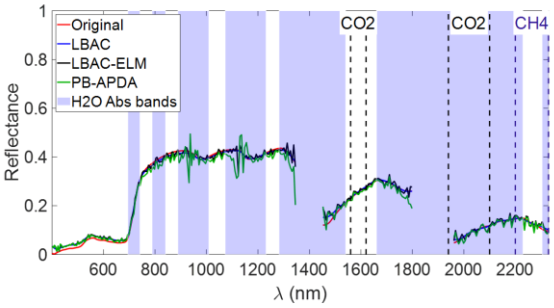

(a)

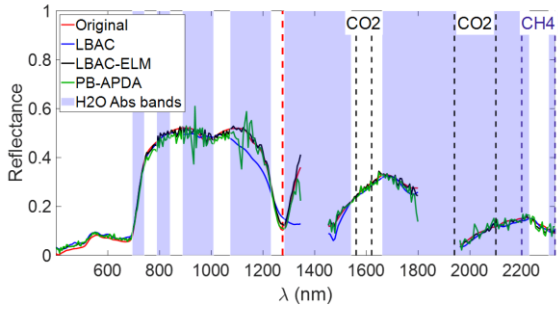

(b)

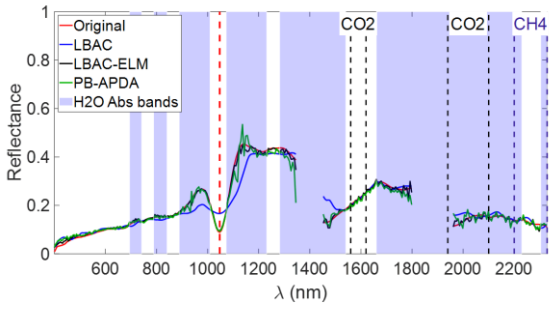

(b)

Figure 5. Examples of estimation provided by LBAC, LBAC-ELM and PB-APDA on three spectra: (a) background; (b) anomalous spectrum 1 and (c) anomalous spectrum 2. In this case SNR=30 dB and a systematic spectral shift equal to $0.2 \cdot FWHM$ *is added to each spectral channel.*

Results in Figure 4 (a) show that the three algorithms provide a good reconstruction of the background reflectance spectrum. In fact, all the estimated spectra fit well the true reflectance curve. As expected, in the two cases of anomalous spectra, the original LBAC algorithm fails in estimating the reflectance especially in correspondence of the narrow band spectral features around 1280 nm (Figure 4 (b)) and 1050 nm (Figure 4 (c)), respectively. Conversely, LBAC-ELM provides good results for both the anomalous spectra. As expected, the PB-APDA also accurately estimate the anomalous spectra. Notice that, as claimed in Section III.B, both LBAC-ELM and PD-APDA, operating the inversion of the RTM, include in the estimated reflectance the high frequency spectral features due to random noise. The latter are instead filtered out by LBAC as evidenced by the more regular behavior of the reflectance estimates.

LBAC-ELM, exploiting the robustness of both LBAC and ELM to systematic errors, is expected to be less sensitive than PB-APDA to that kind of errors. Experimental evidence is provided by the results in Figure 5 (a)-(c) which refer to the same targets considered in Figure 4. They are obtained leaving unchanged the SNR and by simulating a spectral calibration error consisting in a small spectral shift in the sensor channels. Specifically, it is set to $0.2 \cdot FWHM$ for each channel. Results in Figure 5 (b)-(c) show that LBAC-ELM is quite insensitive to the spectral shift. The same conclusion cannot be drawn for PB-APDA. In fact, the estimates provided by that algorithm exhibit high frequency spectral features in addition to those due to random noise. This is particularly evident in the two water vapor absorption bands around 940 nm and 1130 nm. As to LBAC, its robustness with respect to spectral calibration errors is shown in Figure 5 (a), where the estimate provided by the algorithm has the same regular behavior of the true spectrum.

The conclusions drawn from the examples discussed above can be generalized. To give evidence we have performed an extensive analysis, where the three algorithms have been applied to 100 simulated radiance images, which differ in the simulated atmosphere, the noise realizations, and the position and type of anomalous spectra. In each image 50 anomalous targets with size 3x3 pixels were injected.

We first discuss results obtained in absence of spectral calibration errors. Specifically, with reference to three SNR values, in Figure 6 (a)-(c) and Figure 7 (a)-(c) we show, in form of boxplot, the root relative squared estimation error (in percent) defined in eq. (7) and provided by LBAC, LBAC-ELM and PB-APDA in the two cases of: background pixels (Figure 6 (a)-(c)) and small anomalous pixels (Figure 7 (a)-(c)). Each plot provides five indices, with reference to Figure 6: the red line is the median, the edges of the box are the 25th percentile and the 75th percentile, respectively, and the whiskers are the minimum and the maximum values.

As to background pixels, Figure 6 (a)-(c) shows that all the algorithms provide quite accurate estimates of the reflectance data. The estimation errors are lower than 9% for all the considered SNR values. Figure 6 (a) confirms the robustness of LBAC with respect to random noise. The median values of the errors are approximately the same for all the SNR values, although we get a more compact distribution of the error for the highest SNR. LBAC-ELM and PB-APDA attain very similar performance. In both cases, estimation accuracy improves as the SNR increases.

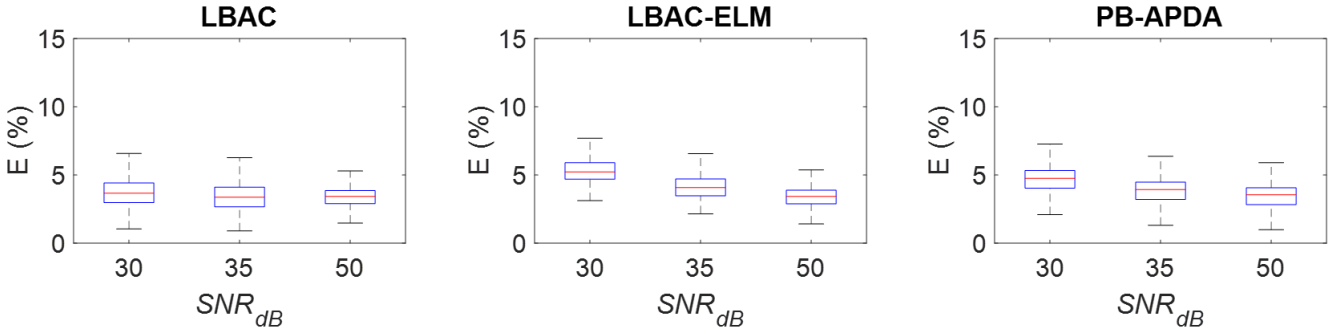

Figure 6. Background pixels for SNR = 30, 35 and 50 dB: boxplot chart of the root relative squared error provided by (a) LBAC, (b) LBAC-ELM and (c) PB-APDA.

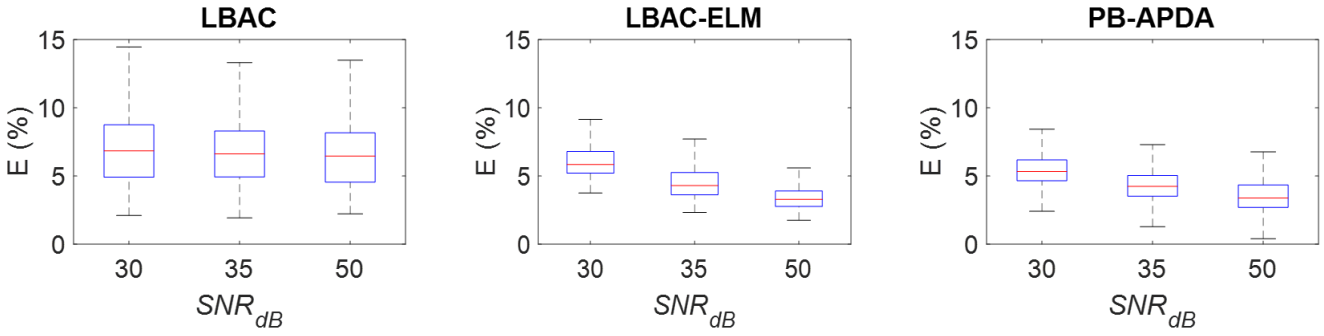

(a) (b) (c)

Figure 7. Anomalous pixels for SNR = 30, 35 and 50 dB: boxplot chart of the root relative squared error provided by (a) LBAC, (b) LBAC-ELM and (c) PB-APDA.

Figure 7 (a), shows that, as expected, LBAC estimation accuracy degrades in the case of anomalous spectra. Regardless of the SNR value, the errors are higher than those obtained for the background pixels. On the contrary, both LBAC-ELM and PB-APDA have a much better behavior as they provide, for anomalous spectra, approximately the same values of errors produced in the case of background pixels. Notice that for all the noisy cases, the errors obtained by the two algorithms have lower median values than LBAC and a more compact distribution. The trend of the error with respect to SNR confirms that both algorithms improve their performance as the SNR increases.

A similar analysis was carried out with respect to systematic errors. In particular, setting $SNR = 50\,dB$, different spectral calibration errors were simulated by adding to the central wavelength of each channel a spectral shift equal to $\alpha \cdot FWHM$ with α ranging from -0.3 to 0.3. Results obtained by the three algorithms and in the cases of background pixels and anomalous spectra are reported in Figure 8 and Figure 9, respectively.

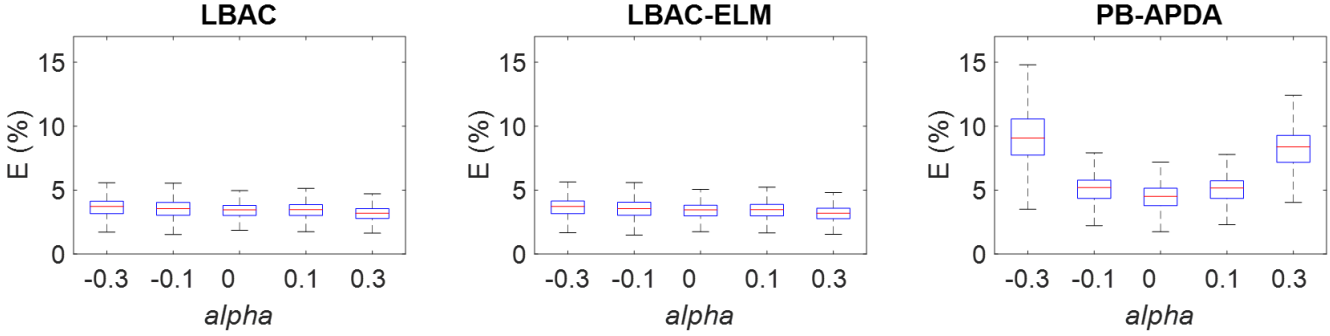

(a) (b) (c)

Figure 8. Background pixels, SNR = 50 dB and spectral shift per channel equal to $\alpha \cdot FWHM$: boxplot chart of the root relative squared error provided by (a) LBAC, (b) LBAC-ELM and (c) PB-APDA.

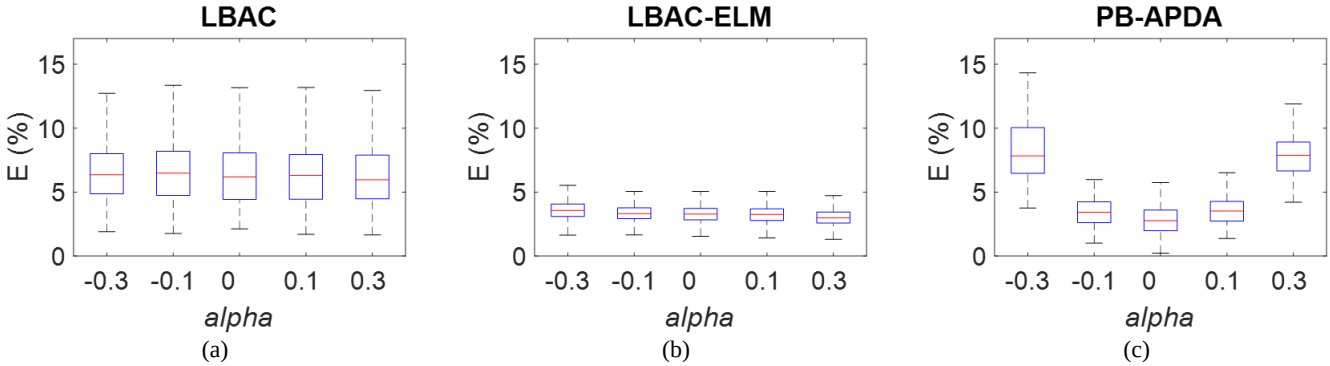

(a) (b) (c)

Figure 9. Anomalous pixels, SNR = 50 dB and spectral shift per channel equal to $\alpha \cdot FWHM$: boxplot chart of the root relative squared error provided by (a) LBAC, (b) LBAC-ELM and (c) PB-APDA.

Figure 8 (a) and (b) show that both LBAC and LBAC-ELM are robust to spectral calibration errors when applied to background pixels. The distribution of the errors provided by the two algorithms are almost stable as the spectral shift varies. In all cases the errors are less than 6%. As opposite, PB-APDA performance (Figure 8 (c)) strongly depends on the systematic

errors. As shown in Figure 8 (c), the estimation errors increase as the absolute value of the spectral shift increases.

As to anomalous pixels, results in Figure 9 confirm: 1) the weakness of LBAC with respect to anomalous spectra (Figure 9 (a)) and 2) the sensitivity of PB-APDA to systematic errors (Figure 9 (c)). LBAC-ELM is the best performing algorithm as it has the lowest error values regardless of the spectral shift (Figure 9 (b)).

As stated in Section III.A, LBAC-ELM leverages the strengths of both LBAC and ELM. Thus, it inherits from the two algorithms the robustness with respect to spectral calibration errors. Results, not discussed here for the sake of brevity, show that this also applies to systematic errors due to imperfect radiometric calibration. This is not true for, PB-APDA and, in general, PB algorithms. With respect to residual radiometric calibration errors, they have the same sensitive shown for the spectral calibration errors.

It is worth noting that, we can state that the robustness property of LBAC-ELM, actually applies to local systematic errors. This is explained by the fact that, in the algorithm, ELM is applied as a post-processing to LBAC in a local fashion. Thus, we can state that LBAC-ELM is robust to those errors that are systematic in the neighborhood adopted for ELM post-processing.

B. LBAC-K performance analysis.

An experimental analysis similar to that discussed above was performed for the scenario concerning the anomalies with known spectral signatures, where LBAC-K algorithm is proposed. In the experiments discussed in this Sub-Section, we simulated 100 radiance images, and in each of them we injected in the background four anomalous spectra with dimensions of 11x11 pixels. Of course, the spectra of those anomalies are considered as known in the application of LBAC-K algorithm.

Figure 10 (a)-(d) show examples concerning one of the simulated radiance images having $SNR = 30\,dB$ and spectral shift equal to $0.2 \cdot FWHM$. We plot the results provided by LBAC-K, LBAC and PB-APDA (for completeness) on the four anomalous spectra in the image.

Figure 10 (a)-(d) show that LBAC-K effectively estimate the spectral reflectance of each anomalous pixel. In particular, we can note that it is robust to both random noise and systematic errors here simulated as a spectral shift. This is due to fact that LBAC-K is an extension of the original LBAC and shares noise robustness with it. Results, also confirm the inability of LBAC in addressing narrow spectral features along with the sensitivity of PB-APDA (and in general PB algorithms) to both random noise and systematic errors.

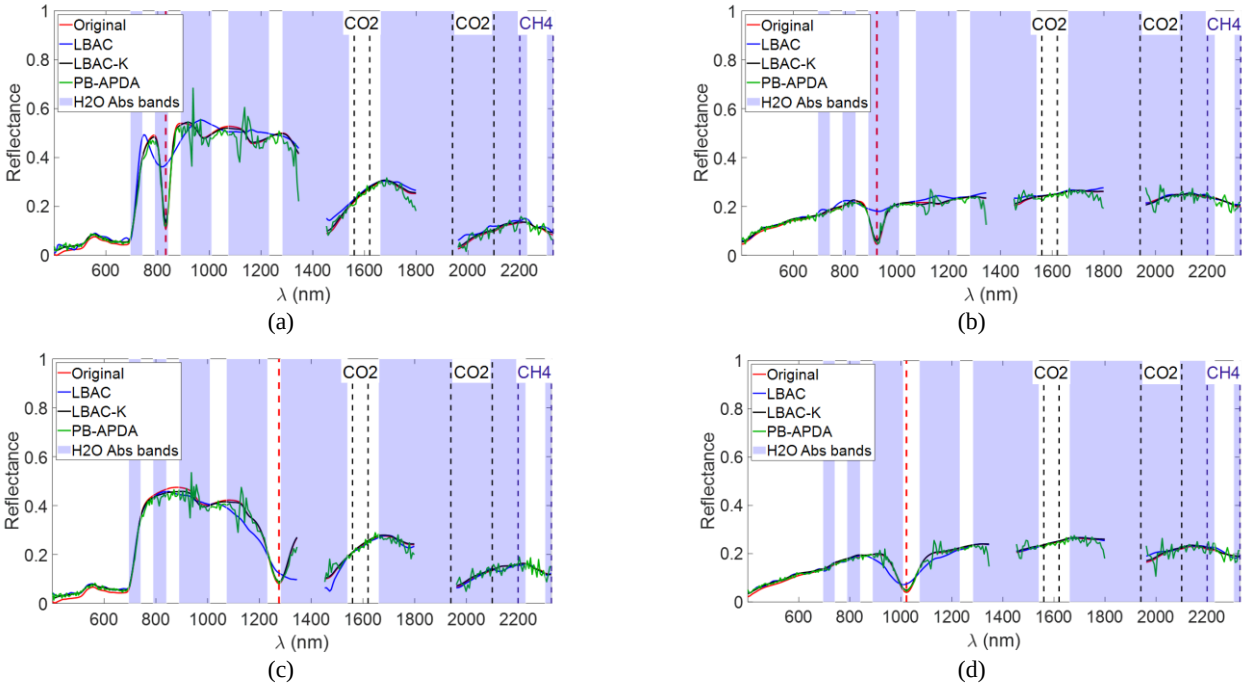

Figure 10. Examples of estimation provided by LBAC, LBAC-K and PB-APDA on four anomalous spectra. In this case SNR=30 dB and a systematic spectral shift equal to $0.2 \cdot FWHM$ *is added to each spectral channel.*

The conclusions drawn from the presented example can be generalized by analyzing the results obtained in all the experiments carried out. Figure 11 (a)-(b) show the boxplot charts for the estimation errors at varying SNR values provided by LBAC-K over both classes of background pixels (Figure 11 (a)) and anomalous pixels (Figure 11 (b)). These results were obtained without spectral systematic errors. The errors provided by LBAC and PB-APDA, in this case, are not represented because they are the same as those discussed in Sub-Section IV.A. It is worth noting, that LBAC-K provides the same low estimation errors (≤8%) for both background and anomalous pixels. The errors values are approximately the same for all the SNR values considered, thus demonstrating the robustness of the method to random noise.

As to spectral calibration errors, robustness of LBAC-K is shown for both background and anomalous pixels in the boxplot charts of Figure 12 (a)-(b). They refer to the case of $SNR = 50dB$ and spectral shift per channel equal to $\alpha \cdot FWHM$ with α in the range $[-0.3, 0.3]$. We can see that, for both classes LBAC-K has almost stable estimation errors for all the considered spectral shift values. Notice that, the errors on the anomalous pixels are slightly lower than those obtained on the background ones. This can be explained by considering that, the estimation error is the combination of two components: that due to the reconstruction of the spectrum on the adopted basis matrix and that due to noise. Since, in the case of LBAC-K, the adopted basis matrix includes the spectra of the anomalous pixels, a lower reconstruction error is expected for those pixels than for the background ones.

To conclude this analysis, let us refer to Figure 13 that shows the errors provided by LBAC and LBAC-K on the background pixels obtained with SNR=30 dB and without spectral shift. We can note that the errors provided by LBAC-K are slightly higher than those of LBAC. This is due to the fact that LBAC-K uses a coding mechanism based on a basis matrix $\mathbf{U}^*$ having rank higher than that adopted by LBAC ($\mathbf{U}$). Specifically, in the experiment discussed in this Sub-Section, $\mathbf{U}^*$ is obtained from $\mathbf{U}$ by adding the four generated anomalous spectra. It is quite intuitive that by increasing the dimension of the reflectance subspace, the number of noise components included in that subspace during the estimation phase also increases. In general, the increase of the rank of the reflectance subspace, corresponds to a reduction in the ability of the algorithm to filter out the noise components.

(a) (b)

Figure 11. LBAC-K: boxplot chart of the errors obtained with SNR= 30,35 and 50 dB (no spectral shift) in the case of (a) background pixels; (b) anomalous pixels.

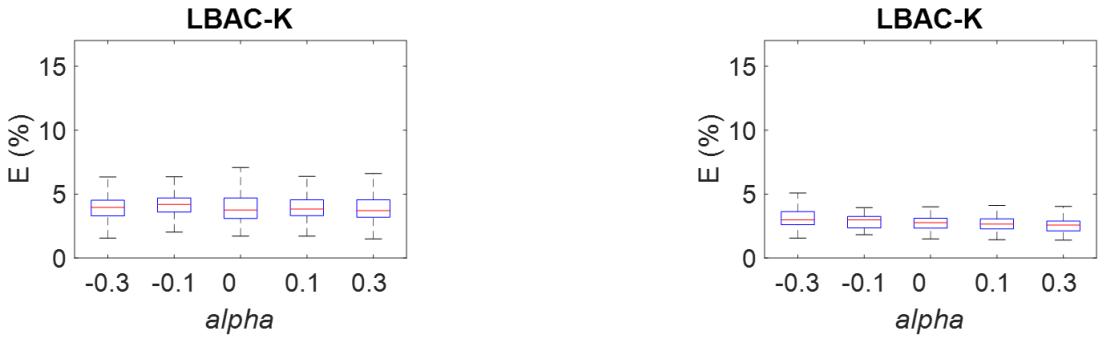

(a) (b)

Figure 12. LBAC-K: boxplot chart of the errors obtained with SNR= 50 dB and spectral shift per channel equal to $\alpha \cdot FWHM$ ($\alpha = -0.3, -0.1, 0, 0.2, 0.3$) in the case of (a) background pixels; (b) anomalous pixels.

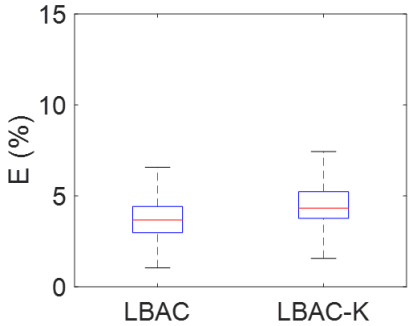

Figure 13. Estimation errors provided by LBAC and LBAC-K on background pixels with SNR=30 dB and without spectral shift.

V. Results on Real Data

In this Section, in order to give an example of real data processing, we discuss results obtained on the radiance image belonging to the SHARE 2012 data set and concerning the rural scene located in AVON already introduced in Section IV and whose RGB representation is shown in Figure 2 (a).

We would like to premise that, in general, an exhaustive analysis of the performance of an AC algorithm over real data is practically unfeasible. It requires an exhaustive ground truth that encompasses the reflectance spectra measured on many

reference targets deployed in the scene. In practice, such an extensive ground truth is unlikely to be available. Thus, simulation remains the only tool for an effective performance assessment in many operational scenarios. However, examples on real data allow us to draw some conclusions about the performance of the algorithms.

Data analyzed in this Section, include an L2 product (spectral reflectance image) obtained by the popular PB atmospheric compensation commercial software package ATCOR4 ([5]). Specifically, the L2 product made available, consists in spectral reflectance data obtained after a polishing process performed by ATCOR4. Polishing, is generally used to filter the reflectance data with the aim of reducing the effects of random noise and systematic errors in the acquired radiance image. It relies on the same hypothesis as that considered in deriving LBAC, i.e. the spectral reflectances of many natural and man-made materials are "smooth" in the sense that they have a lower rate of change than that typically observed in the radiance data. Polishing shares with LBAC the same drawbacks related to the representation of anomalous spectral features. Therefore, the polished spectral data provided by ATCOR4 are useful for evaluating the effectiveness of the proposed algorithms in most of the image pixels, those indicated as background in this paper. On the contrary, they are probably not suitable for showing the performance on anomalous pixels.

Fortunately, during the experimental campaign, the reflectances of some targets deployed in the scene were measured by the Analytical Spectral Devices (ASD) FieldSpec Pro instrument (https://www.rit.edu/cos/share2012/asd.php). One of those spectra concerns a tarp (named T_1, hereinafter) located in the upper side of the scene (*Figure 2* (a)), which, indeed has "anomalous" spectral features. Figure 14 (a), shows the detail of the region of the scene that includes the tarp and highlights its location (red dot). While Figure 14 (b) shows the spectral reflectance of the tarp and highlights three specific anomalous spectral features (F_1, F_2, F_3) that will be considered in comparison of the results of the algorithms.

LBAC, LBAC-ELM and LBAC-K are applied to the above introduced radiance data. The basis matrix **U** adopted by LBAC and LBAC-ELM has rank 40. The window for LBAC-ELM has size 11x11 pixels. LBAC and LBAC-ELM are exactly the same as adopted in the previous presented experiments (Section IV). As to LBAC-K, being interested here in the target named T1, it is applied by using as anomalous spectrum that of T1 (Figure 14 (b)) included in the ground truth of the SHARE 2012 data set.

For completeness, we also apply to the data the PB-APDA algorithm introduced in Section IV.

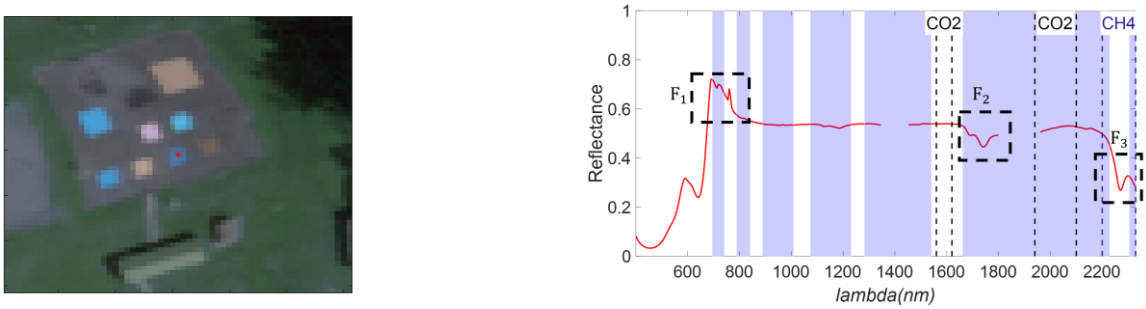

(a) (b)

Figure 14. (a) Detail of the region of the scene that includes the anomalous target, i.e. tarp. (b) spectral reflectance of the tarp T_1 measured by the ASD FieldSpec Pro instrument. Three spectral features (F_1, F_2, F_3) are highlighted.

With reference to T_1, Figure 15 compares the reflectance estimates provided by the algorithms with the ground truth. For better clarity, we have separated the results provided by LBAC and its modifications (Figure 15 (a)) from those obtained by the PB methods (Figure 15 (b)).

We can note that, although LBAC estimate (Figure 15 (a)) follows the general trend of the true spectra, it over-smooths some specific features such as those denoted as F_1, F_2 and F_3. Furthermore, it does not correctly follow the spectral feature located around 700 nm. Results improve by applying both the modified versions of LBAC proposed in this paper. As expected, the estimate provided by LBAC-ELM exhibits high frequency components basically due to random noise. Those components vanish in the estimate obtained by LBAC-K. As to ATCOR4 (Figure 15 (b)), we can note that the spectral features F_2 and F_3 are accurately reconstructed. This conclusion does not apply to the feature F_1, which is probably distorted by the polishing process. PB-APDA provides the worst estimate probably due to its sensitivity to residual calibration errors in the data.

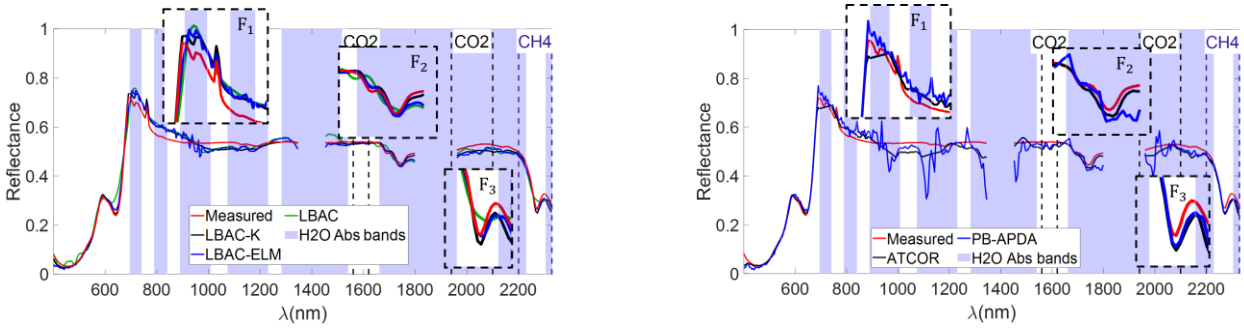

(a) (b)

Figure 15. T_1:(a) reflectance estimates provided by LBAC, LBAC-ELM and LBAC-K, (b) reflectance estimates provided by the PB methods ATCOR4 (+spectral polishing) and PB-APDA. In the two figures the spectral reflectance measured by the ASD FieldSpec Pro instrument is also shown.

For completeness, to give a visual example, in Figure 16 (a)-(c) we show the estimates provided by all the algorithms on three background pixels taken from a vegetated area (Figure 16 (a)), the white panel at the top of the scene (Figure 16 (b)) and a paved road (Figure 16 (c)).

As a general remark, we can say that the estimates provided by ATCOR4, LBAC, LBAC-ELM and LBAC-K are very similar. We can once again see the major sensitivity of LBAC-ELM to random noise affecting the data, especially in the water absorption band around 940 nm. On the contrary, ATCOR4 (thanks to spectral polishing), LBAC and LBAC-K are more robust to random noise.

The worst results are attained by PB-APDA. The spectral features exhibited by the estimates provided by PB-APDA in the regions around 940 nm, 1100 nm and 2100 nm seem to be systematic and led us to believe that they are due to residual spectral or radiometric calibration errors. This observation, along with the absence of those spectral features in the estimates provided by LBAC and its modifications, can be viewed as an indirect demonstration of the robustness of the learning-based approach to systematic errors in the radiance data.

An overall comparison of the results provided by the algorithms on all the pixels of the image, is shown in Figure 17, where the root relative squared error (in percent) between the estimates of each algorithm and those provided by ATCOR4 (here assumed as reference) are reported. We can note that all the algorithms have estimation errors (w.r.t ATCOR4) lower than 11%. LBAC and LBAC-K provide reflectance spectra very similar to those of ATCOR4 (the error is lower than 7%). LBAC-ELM due to the effects of random noise, provides slightly different reflectance estimates. PB-APDA provides less similar estimates with respect to ATCOR4, probably as a consequence of both random noise and systematic errors in the data.

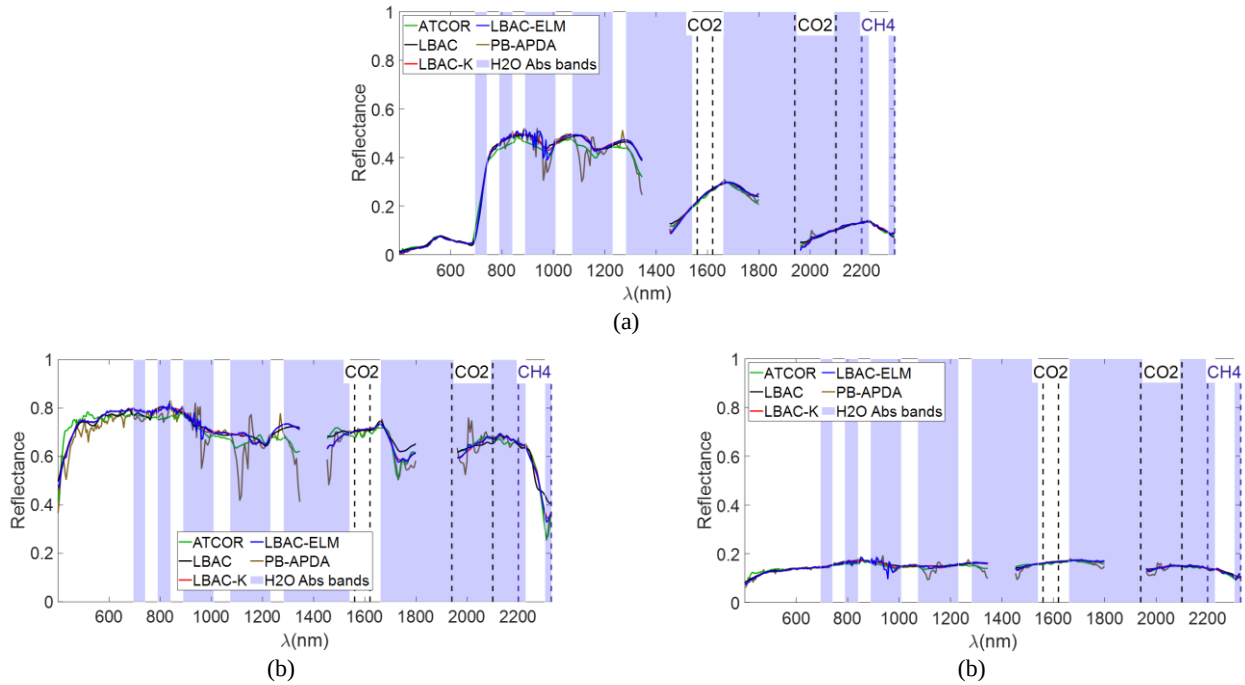

(a)

(b) (b)

Figure 16. Examples of estimation provided by ATCOR4, LBAC, LBAC-ELM and PB-APDA on three background pixels taken on: (a) vegetated area; (b) white panel at the top of the scene (c) paved road.

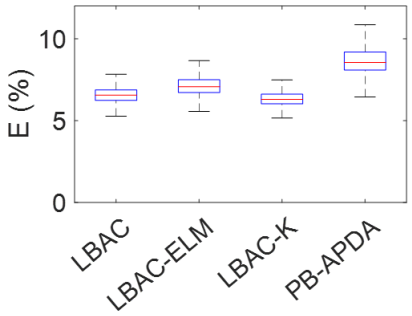

Figure 17. Boxplot chart of the root relative squared error (in percent) between the estimates provided by LBAC, LBAC-ELM, LBAC-K, PB-APDA and ATCOR4. The latter is assumed as reference.

VI. Conclusions

In this paper we have extended the LBAC approach proposed in [19] in order to improve its performance with respect to anomalous spectral features. Two solutions have been introduced with reference to two different scenarios which are of interest in many hyperspectral data exploitation applications. The first solution (LBAC-ELM) refers to small and rare anomalous pixels and could be of interest in many applications such as man-made targets detection. The second solution (LBAC-K) relies on the knowledge of the spectral reflectance of the anomalous material and has its impact in applications such as mineral exploration and contaminants detection.

An extensive analysis has been carried out on simulated data to discuss the limitations of the original LBAC and the improvements due to the proposed updates. An example over real data has also been discussed to provide a proof of concept for the algorithms proposed.

Results have shown the effectiveness of the two solutions and have confirmed the robustness of LBAC and its modifications to systematic errors in the analyzed radiance data. This makes the learning-based approach a promising tool for atmospheric compensation of hyperspectral data.

It is worth noting that, LBAC (and its modifications) can be viewed as a cognitive algorithm whose memory (spectral library data base) could be enriched or modified by *a priori* knowledge in order to match the specific characteristics of the scene under analysis. For instance, you can think to an "application-driven" spectral library that is populated or enriched with specific spectra of interest in the considered application scenario. This is just an example of the actions we can take for improving the effectiveness of the approach. It is quite general and regression models and/or encoding mechanisms different from those adopted in this work can be used to further improve its ability and manage more complex structures in the data.

Despite the promising results of the learning-based approach discussed in this paper, some open issues still remain that need further investigation. For instance, further efforts are required to improve the performance of LBAC and of its modified versions to include the effects of a) terrain elevation, b) anisotropic response of the surface to the incident radiation, c) more complicated aerosol profiles. Moreover, the performance of the approach with respect to those applications not included in the two scenarios discussed in this work needs to be further investigated.

References

[1]. J. R. Schott, Remote Sensing: The Image Chain Approach, 2nd ed., New York: Oxford University Press, 2007.

[2]. M. K. Griffin and H. K. Burke, "Compensation of Hyperspectral Data for Atmospheric Effects," Lincolm Laboratory Journal, Vol. 14, No. 1, pp. 29-54, 2003.

[3]. B. -C. Gao, K. B. Heidebrecht, and A. F. H. Goetz, "Derivation of scaled surface reflectances from AVIRIS data," Remote Sensing of Environment, Vol. 44, pp. 165−178, 1993.

[4]. F. A. Kruse, "Comparison of ATREM, ACORN, and FLAASH atmospheric corrections using low-altitude AVIRIS data of Boulder, CO," Summaries of 13th JPL Airborne Geoscience Workshop, Jet Propulsion Lab, Pasadena, CA. (2004).

[5]. R. Richter and D. Schlaepfer, "Geo-atmospheric processing of airborne imaging spectrometry data. Part 2: atmospheric/topographic correction," International journal of Remote Sensing, Vol. 23, No. 1, pp. 2631-2649, 2002.

[6]. N. Acito, M. Diani, "Unsupervised Atmospheric Compensation of airborne hyperspectral images in the VNIR spectral range," IEEE Trans. on Geoscience and Remote Sensing, Vol. 56, No. 7, pp. 3924-3940, 2018.

[7]. E. J. Ientilucci, S. Adler-Golden, "Atmospheric compensation of hyperspectral data: An overview and review of In-Scene and Physics-Based approaches," IEEE Geoscience and Remote Sensing Magazine, Vol. 7, No.2, pp. 31-50, June 2019.

[8]. D Schlaepfer, C. C. Borel, J. Keller and K. I. Itten, "Atmospheric Precorrected Differential Absorption Technique to Retrieve Columnar Water Vapor," Remote Sensing of Environment, Vol. 65, No. 3, pp: 353-366, Sept. 1998.

[9]. M. Griffin and H. Burke, "Compensation of hyperspectral data for atmospheric effects," Lincoln Laboratory Journal, Vol. 14, no, 1, pp. 29-54, 2003.

[10]. L. Bernstein, X. Jin, B. Gregor and S. Adler-Golden, "The quick atmospheric correction (QUAC)," in Proc. 4th Workshop on Hyperspectral Image and Signal Processing: Evolution in Remote Sensing (WHISPERS), Shangai, China, 2012.

[11]. G. Ferrier, N. S. Trahair, "Evaluation of apparent surface reflectance estimation methodologies," Int. Journal of Remote Sensing, Vol. 16, No. 12, pp. 2291-2297, Dec. 1995.

[12]. W. M. Baugh, D. P. Groeneveld, "Empirical proof of empirical line," Int. Journal of Remote Sensing, Vol. 29, No. 3, pp. 665-672, March 2008.

[13]. F. Kruse, "Use of airborne imaging spectrometer data to map minerals associated with hydrothermally altered rocks in northern Grapevine Mountains, Nevada and California," Remote Sensinf Environment, Vol. 24, No. 1, pp. 31-51, Feb. 1988.

[14]. C. J. Miller, "Performance assessment of ACORN atmospheric correction algorithm," in Proc. SPIE Algorithms and Technologies for Multispectral, Hyperspectral, and Ultraspectral Imagesy VIII, Vol. 4725, Orlando, FL, pp. 438-449, 2002.

[15]. S.M. Adler-Golden, A. Berk, L.S. Bernstein, S. Richtsmeier, P.K. Acharya, M.W. Matthew, G.P. Anderson, C. Allred, L. Jeong, and J. Chetwynd, "FLAASH, A MODTRAN4 Atmospheric Correction Package for Hyperspectral Data Retrievals and Simulations," Proc. 7th Ann. JPL Airborne Earth Science Workshop, JPL Publication 97-21, Pasadena, Calif., pp. 9–14, 1998.

[16]. R. de los Reyes, M. Langheinrich, P. Schwind, R. Richter, B. Pflug, M. Bachmann, R. Müller, E. Carmona, V. Zekoll, P. Reinartz, "PACO: Python-Based Atmospheric Correction," Sensors 2020, 20, 1428.

[17]. D. R. Thompson, K. N. Babu, A. J. Braverman, M. L. Eastwood, R. O. Green, J. M. Hobbs, J. B. Jewell, B. Kindel, S. Massie, M. Mishra, A. Mathur, V. Natraj, P. A. Townsend, F. C. Seidel, M. J. Turmon, "Optimal estimation of spectral surface reflectance in challenging atmospheres," Remote Sensing of Environment, Vol. 232, pp. 1-15, 2019.

[18]. A. Berk, L. S. Bernstein and D. C. Robertson, "MODTRAN: A Moderate Resolution Model for LOWTRAN 7," Spectral Sciences, Burlington, MA, GLTR890122, 1989.

[19]. N.Acito, M. Diani, G. Corsini, "Learning-based approach for atmospheric compensation of VNIR hyperspectral data," IEEE Trans. on Geoscience and Remote Sensing, Vol. 59, No. 5, pp. 4218-4232, May 2021.

[20]. A.M. Baldridge, S.J. Hook, C.I. Grove and G. Rivera, "The ASTER Spectral Library Version 2.0," Remote Sensing of Environment, Vol 113, pp. 711-715, 2009.

[21]. R.N. Clark, G.A. Swayze , R.A. Wise, K.E. Live, T.M. Hoefen, R.F. Kokaly, and S.J. Sutley, USGS Digital Spectral Library splib06a: U.S. Geological Survey Data Series 231, 2007.

[22]. Available on line at http://opticleaf.ipgp.fr/index.php?page, last accessed December 2020.

[23]. D. R. Thompson, L. Guanter, A. Berk, B.-C. Gao, R. Richter, D. Schläpfer, K. J. Thome, "Retrieval of Atmospheric Parameters and Surface Reflectance form Visible and Shortwave Infrared Imaging Spectroscopy Data," Surv Geophys 40, 333–360, May 2019.

[24]. D. Schläpfer, R. Richter, "Spectral polishing of high resolution imaging spectroscopy data," Proceedings of the 7th SIG-IS workshop on imaging spectroscopy, Edinburgh, UK, p 7. http://www.daniel-schlaepfer .ch/pdf/Schla epfer IS2011_polis h.pdf

[25]. A. Hueni, J. Nieke, J. Schopfer, M. Kneubuhler, K.I. Itten, "The spectral database SPECCHIO for improved long-term usability and data sharing," Elsevier Computers and Geosciences, Vol. 35, No. 3, pp. 557-565, March 2009.

[26]. A. Giannandrea, N. Raqueno, D. W. Messinger, J. Faulring, John P. Kerekes, et al., "The SHARE 2012 data campaign," in Proc. SPIE, vol. 8743, pp. 87430F-1-15, 2013.

[27]. https://www.rit.edu/cos/share2012/, last accessed December 2020.

[28]. T. Skauli, "Sensor noise informed representation of hyperspectral data, with benefits for image storage and processing," Optics Express, Vol. 19, No. 14, pp. 13031-13046, June 2011.

[29]. N. Acito, M. Diani, G. Corsini, "Signal-Dependent Noise Modeling and Model Parameter Estimation in Hyperspectral Images," IEEE Trans. on Geos. and Rem. Sensing, Vol. 49, No. 8, pp. 2957-2971, August 2011.